8-2010

The Synthesis and Crystal Chemistry of Ca12Al14O33 doped with Fe2O3

Sabina Nwamaka Ude
University of Tennessee - Knoxville, sude@utk.edu

To the Graduate Council:

I am submitting herewith a thesis written by Sabina Nwamaka Ude entitled "The Synthesis and Crystal Chemistry of Ca12Al14O33 doped with Fe2O3." I have examined the final electronic copy of this thesis for form and content and recommend that it be accepted in partial fulfillment of the requirements for the degree of Master of Science, with a major in Materials Science and Engineering.

Claudia J. Rawn, Major Professor

We have read this thesis and recommend its acceptance:

Carl J. McHargue, Thomas T. Meek

Accepted for the Council:
Dixie L. Thompson

Vice Provost and Dean of the Graduate School

(Original signatures are on file with official student records.)

To the Graduate Council:

I am submitting herewith a thesis written by Sabina Nwamaka Ude entitled "The Synthesis and Crystal Chemistry of $Ca_{12}Al_{14}O_{33}$ doped with Fe_2O_3". I have examined the final electronic copy of this thesis for form and content and recommend that it be accepted in partial fulfillment of the requirements for the degree of Master of Science with a major in Materials Science and Engineering.

Claudia J. Rawn, Major Professor

We have read this thesis

and recommend its acceptance:

Carl J. McHargue

Thomas T. Meek

Accepted for the Council:

Carolyn R. Hodges

Vice Provost and Dean of the Graduate School

(Original signatures are on file with official student records.)

The Synthesis and Crystal Chemistry of

$Ca_{12}Al_{14}O_{33}$ doped with Fe_2O_3

Thesis presented partial fulfillment for
the Master of Science
Degree
The University of Tennessee, Knoxville

Sabina Nwamaka Ude
August 2010

ABSTRACT

The crystal chemistry of Fe doped mayenite ($Ca_{12}Al_{14-x}Fe_xO_{33}$) samples prepared using solid state and sol-gel synthesis techniques were compared. Five samples were prepared using solid state process with varying Fe concentration (x) where x = 0, 0.05, 0.1, 0.25 and 0.3; two sets of samples were made via the sol-gel, the first set was prepared for studying the amount of Fe substituted by varying the Fe concentration where x = 0, 0.05, 0.1, 0.2, 0.3 and 0.4 and the second set was prepared for studying the firing temperature and did not contain Fe additions (x = 0). Samples produced via the sol-gel method were more likely to be single phase with incorporation of Fe_2O_3 while solid state samples contained multiple phases over the same range of Fe_2O_3 substitutions. The refined lattice parameters, of samples prepared using both methods were observed to increase with increasing Fe concentration, suggesting Fe is replacing Al since Fe has larger ionic radii than Al. Samples prepared via the sol-gel method were found to be single phase at lower temperatures compared to samples prepared via solid state synthesis. Samples synthesized using the sol-gel method were found to have multiple phases when fired at 800 ˚C but were single phase when fired at 900˚C. In comparison, samples synthesized using traditional solid state techniques showed single phase when fired at a temperature of 1350˚C.

TABLE OF CONTENTS

Content **Page**

LIST OF FIGURES

Figure **Page**

LIST OF TABLES

Table **Page**

CHAPTER ONE
INTRODUCTION

1.1 Photovoltaic devices and the role of transparent conductive oxides in photovoltaic devices.

Photovoltaics (PVs) are arrays of cells containing a solar photovoltaic material (i.e. a semiconductor that converts photons from the sun into electricity) that converts solar radiation to direct current electricity. Materials presently used for photovoltaics include mono-crystalline silicon, polycrystalline silicon, microcrystalline silicon, cadmium telluride, and copper indium selenide or sulfide [1]. The high efficiency devices commonly use single crystal silicon grown on crystalline substrates. Some of the substrates used are multi-crystal silicon, SiO_2, graphite, amorphous carbon, AlN, BN, etc. Photovoltaic cells contain light absorbing material in the middle of the cells converting photons into carriers via the photovoltaic effect, different photovoltaic technologies are identified by the composition of this absorbing material. As the carriers are generated, they are separated into electrons and holes and then collected at the contacts. Figure 1 shows a schematic of the generic structure and operation of a single-junction inorganic solar cell.

Drift and diffusion are the two main means of carrier separation. Drift of charge carriers is driven by the built-in electrostatic field of a p-n junction while diffusion is driven by an electrochemical potential gradient causing carriers to move from regions of high to low charge carrier concentration. High efficiency devices depend on diffusion for carrier transport to the junction for collection; it is also the dominant transport mechanism for dye or organic solar cells [2]. Drift is typical of inorganic cells, they are normally p-n junction devices; when drift is important, the structure of the cell can be used to compensate for poor diffusion, for instance, in the depletion region.

The contacts and window layers are critical in shaping the performance of these devices. The contact should be electrically conducting and transparent to photons in the spectral range where the absorber creates carriers. Transparent Conducting Oxides (TCOs) are being used for this purpose in solar cells. TCOs function simultaneously as a window layer, enabling light to reach

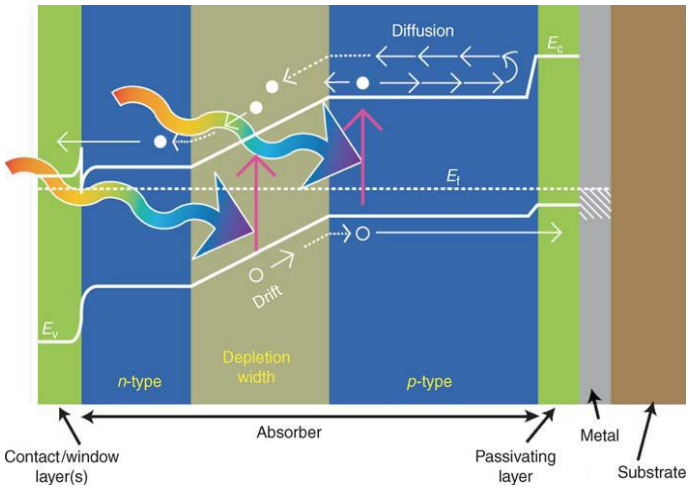

Figure 1. Schematic of a p–n junction solar cell [2].

the active absorbing material, and as an ohmic contact, transporting photo-generated charge carriers away from the absorber [2].

TCOs are characterized by a unique combination of low electrical resistivity and high optical transparency in the visible range of the electromagnetic spectrum. They are an important class of inorganic materials found in nearly every thin film PV device; the thin films of TCOs are used as the electrodes of a wide range of devices including flat-panel displays, electro-chromic windows, and emerging applications such as flexible and invisible electronics [3]. Desired properties of the TCO layer include a sheet resistance < 15 Ω/mm^2 and an average light transmission greater than 80% in the visible region to ensure a contact resistance and high light absorption by the active semiconductor layers. Also a textured surface is desired to achieve gradient refractive index and sufficient light trapping, which are desired electro-optical properties.

The established TCOs have similar carrier generation mechanisms and also similar chemical, electronic and structural properties. These are mainly oxides of transition and post-transition metals with closed packed structures and either four or six-fold coordinated metal ions [3]. A very important feature for the host electronic band structure is a highly dispersed band at the bottom of the conduction band; this is responsible for the high mobility of carriers due to their small effective masses and low optical absorption plus a pronounced Burstein-Moss shift [4, 5].

When doped, and the impurity band overlaps the edge of the conduction band, a degenerate semiconductor is formed which exhibits high transparency in the visible light range and high electrical conductivity. Shown in Figure 2, when the concentration of the impurity is small, the Fermi energy (E_F) appears below the conduction band whereas for high impurity concentration, the energy is above the conduction band edge.

1.2 Transparent conducting oxides

The dual property of transparency and conductivity in oxides was first observed in 1931 in tin oxide (SnO_2), a decade later the first SnO_2 based films on glass were patented and employed as windshield de-icers in World War II [2]. This was followed by the development of Sn-doped indium oxide (ITO) with conductivities on the order of 1-104 S/cm and excellent optical properties [2]. In the last decade, the rise in demand for the devices with TCOs has pushed the industry to undergo a major expansion. These devices include flat panel displays (FPD), light-emitting devices (LED), and solar cells. The expanding use of TCO materials, especially for the production of transparent electrodes for optoelectronic device applications, has developed into a worldwide multi-billion $US economy that in general depends on the availability of ITO. This economy is endangered by the scarcity and high price of In. This situation drives the search for alternative TCO materials to replace ITO, and motivates an intensive investigation of the physics and chemistry of TCO materials [6]. ZnO is one of a select group of materials currently being considered to compete with ITO and SnO_2, ITO has been the most widely utilized, because of its low resistivity and high transmittance. ITO along with SnO_2:F (FTO) and ZnO:Al (AZO) are still the most used and widely studied transparent conductors among the oxides [7]. Although ZnO and SnO_2 have been regarded as promising materials, it is also necessary to develop and optimize new TCO materials for expanding application usage [8]. A large number of alternative binary oxides have been under exploration for the last couple of decades, including Cd_2SnO_4, Zn_2SnO_4, $MgIn_2O_4$, $ZnSnO_3$, $GaInO_3$, $Zn_2In_2O_5$ and $In_4Sn_3O_{12}$. Many of these materials have shown some improvement in properties over the established commercial ones (ITO, AZO, FTO) although none of them to date has shown sufficient overall properties to clearly replace these established ones [7]. There is also interest in conducting layers exhibiting optical transparency into the ultraviolet range for solar cell applications.

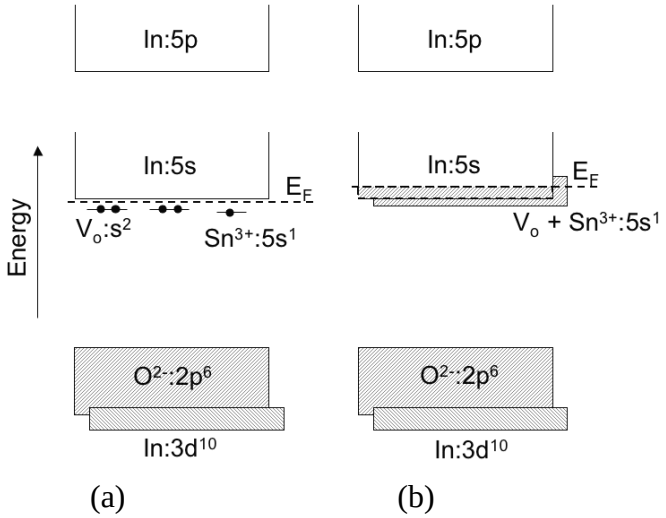

Figure 2. Schematic representation of energy band model for Indium Tin Oxide (ITO) for (a) small and (b) large donor levels [5].

Nevertheless, In_2O_3 based films are still presently the dominant TCO and the FPD industry utilizes more ITO than any other industry. In addition, the photovoltaic industry continues to grow at a steady pace of 25-30% year. It is expected that the demand of these two combined markets will increase beyond the production of indium in the near future. Figure 3 shows the rapid increase in indium consumption in recent years. A representation of the world's mineral resources in common use is shown in Figure 4 and the earth is estimated to contain only about 0.1 ppm of indium making its abundance similar to that of Ag, however, it is nearly three times more expensive by weight than Ag [3]. The high cost of In, coupled with the growing realization that the properties required of TCOs are dependent on the PV technology under consideration, is driving research into alternative materials and processes for manufacturing TCOs for specific applications [2].

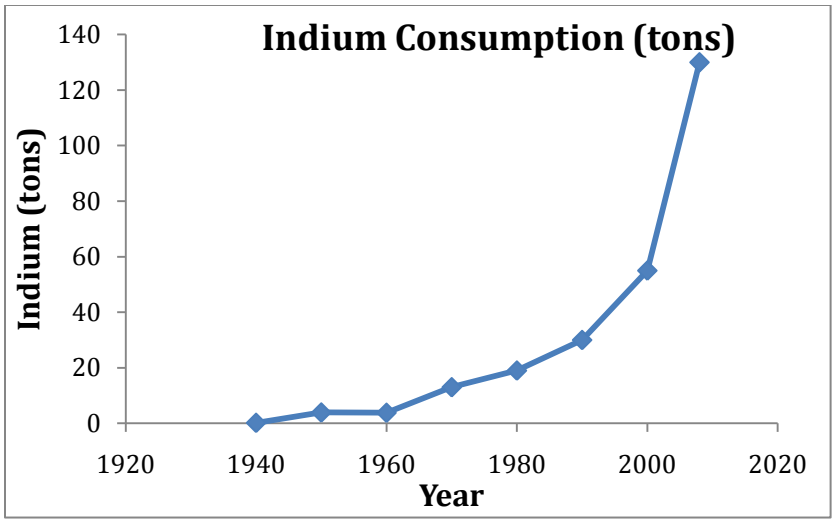

Figure 3. Representation of the appearent consumption of indium [9].

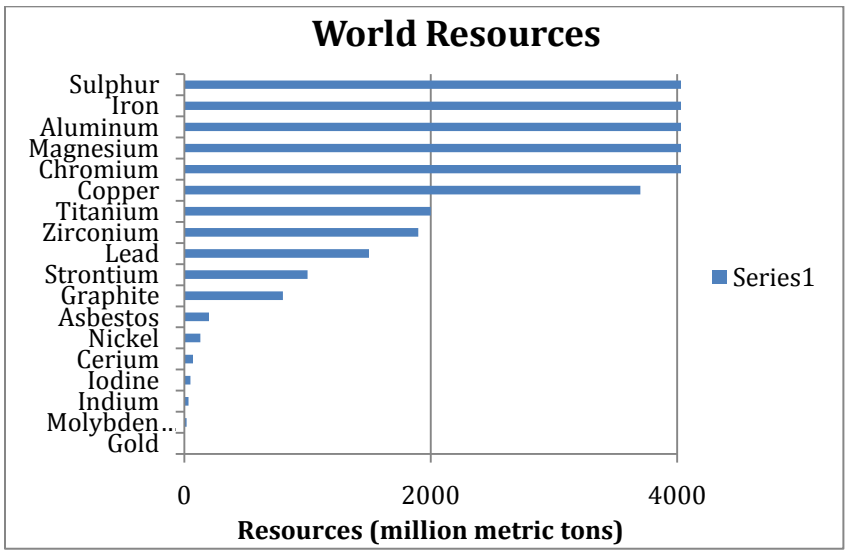

Figure 4. Graph of the world's avaliable mineral resources [9].

1.3 Mayenite as a transparent conducting oxide

The mineral mayenite, known for a long time as a major constituent of calcium aluminate cements with the formula $12CaO \bullet 7Al_2O_3$ or $Ca_{12}Al_{14}O_{33}$, was originally reported from the Eifel volcanic complex in Germany. It is also found at pyrometamorphic sites like in the Hatrurim Formation and in some burned coal dumps [10]. It has recently attracted much attention as a TCO, a catalyst for the combustion of volatile organic compounds, and an ionic conductor.

In 1988 the unusual electrical properties displayed by mayenite were first reported by Lacerda et al. [11] after they found that at high temperatures, as-prepared mayenite had an oxide ion conductivity not far below that of yttria-stabilized zirconia (YSZ). In 2002, mayenite was also reported to be rendered conductive by hydrogen doping and subsequent ultra violet light irradiation [12]. More recently Matsuishi et al. have shown that electron anions have been incorporated leading to the TCO properties of the material. Mayenite has also been discussed as an inorganic electride [13-15].

The new discoveries about mayenite gave way to the reconsideration of main group metals to be used in TCO materials. In striking contrast to the conventional process for designing TCOs, this approach requires the host material be an insulator with a band gap greater than 6.2eV and a concentration of impurities (e.g. H^-, OH^-, Cl^-) large enough so the overlap of their electronic wave functions will form an impurity band inside the gap [3]. The impurity band leads to high carrier mobility due to the extended nature of these states, resulting in relatively low scattering. Furthermore, if the impurity band is narrow enough (< 1.8eV) the intra-band transitions will be kept below the visible range, as well as the plasma frequency. Unlike the commonly used materials for TCO applications, where due to the inter-band transitions from the partially occupied band at the top of the conduction band, 100% transparency can never be achieved; this approach suggests that the combination of 100% optical transparency and high electrical conductivity may be possible [3]. Table 1 is a summary of the comparative cost calculations between ITO and mayenite if used individually as TCO for a solar cell over an area of 12.192m X 6.096m with material thickness of 0.6μm.

1.4 Properties and structure of mayenite

Mayenite is an attractive material because it is thermodynamically stable with a relatively low melting point, 1390-1400°C. Figure 5 shows the binary phase diagram for the system CaO-Al_2O_3 (PDFC # 231, volume 1). $Ca_{12}Al_{14}O_{33}$ is a congruently melting compound and as such, a single crystal can be grown directly from the melt. The materials properties observed in mayenite are related to its particular crystal structure, which may be described as a nano-porous cubic structure. It has a body centered cubic crystal structure belonging to the *I*-43*d* (number 220) space group with a = 11.989 Å and Z =2 [12]. The formula $Ca_{12}Al_{14}O_{33}$ refers to a unique feature

of anion diffusion process, 64 of the 66 oxygen ions per unit cell are fixed in a Ca-Al-O framework forming 12 "cages" [16].

Figure 6 shows the cage-like structure of mayenite with 12 cages per unit cell. The cages are about 5 Å in diameter and the openings between them are about 3.5 Å. It is believed that these openings control the mass transport between the inner cages and the outside. The lattice shows charge neutrality due to the free oxygen ions present in the lattice in addition to the lattice framework, the formula can be written as

$$[Ca_{24}Al_{28}O_{32}] + 2O^{-2} \qquad (1)$$

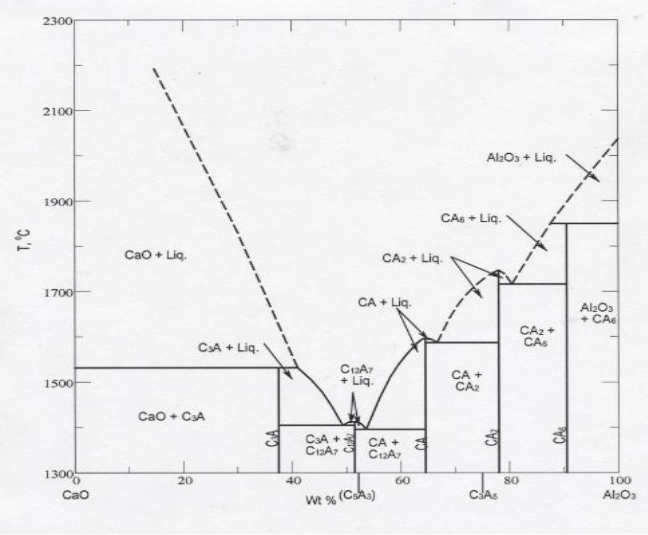

Figure 5. The CaO-Al_2O_3 binary phase diagram (PDFC #231, vol. 1).

Table 1. Comparative cost calculation between ITO and mayenite.

	ITO	12CaO	$7Al_2O_3$	Mayenite
Density (g/cm^3)	7.16	3.35	3.89	3.6078 (ave)
Volume (cm^3)	44.5935	23.3021	21.2915	44.5935
Mass (g)	319.289	78.0619	82.824	160.886
Price ($)	2,171.17	6.48	9.94	16.42

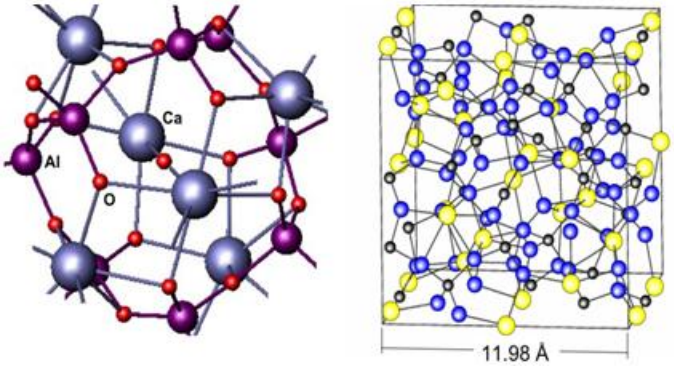

(a) (b)

Figure 6. (a) A cage of $Ca_{12}Al_{14}O_{33}$, (b) unit cell of $Ca_{12}Al_{14}O_{33}$ containing 12 cages [3].

On average each cage has a mean effective charge of +1/3, so the free oxygen anions compensate this positive charge of the framework and are coordinated to the 6 Ca^{2+} cations forming the cage walls along with the Al^{3+} cations. The oxygen ions are loosely bound to the framework because of the spacing between them and the closest Ca^{2+} is about 1.5 times bigger than the sum of their effective radii. The cage concentration is 7.0 – 1021 cm^{-3} thereby providing the flexibility for the replacement of the free O^{2-} ions with other anions such as fluoride, chloride, hydroxides or hydride, as well as electrons, forming electrides [17].

1.5 Electrides

Electrides are materials that trap electrons at a stoichiometric concentration in the solid state [17]. Chemically, trapped electrons can be viewed as the smallest possible anion, and such materials could serve as strong reducing agents. Mayenite, viewed as a nano-porous oxide, provides a structure in which oxide anions can be partially replaced by electrons, and retain thermal stability, even under ambient atmosphere [12]. Electrides are able to combine transparency with electronic conductivity, making them useful for flat panel displays and electronic devices. Their electronic properties range from superconductivity, at high electron concentrations, to semiconductivity, at low electron contents. Crystalline electrides may be viewed as stoichiometric F–centers where all ionic sites have trapped electrons. F-centers are generated when a low concentration of electrons has been trapped at anion vacancies. The structure of the electrides determines the mobility of the trapped electrons; this movement is

influenced by both the size and length of the cavities or channels that connect the different anion sites.

Prior to the work on mayenite, all electrides made to date have been organic and the key to their synthesis is the capture of the cation in an alkali metal solution by a non-reducible complexant, usually a crown ether, a cryptand (molecular entity comprising a cyclic or polycyclic assembly of binding sites containing three or more binding sites held together by covalent bonds), or their nitrogenous analogs. The thermal instability combined with the difficulty to grow large samples of these compounds has been the major impediment to study their properties [3]. From a physics standpoint, the stabilization of numerous bound electrons, or F-centers, could provide new approaches to preparing conductive materials with unusual optical or magnetic properties [12].

1.6 Mayenite activation processes

The two main activation processes have been discovered which render mayenite conductive:

- Hydrogen-doping/hydrogen-implantation followed by ultra violet (UV) light irradiation.
- Removal of the free O^{2-} species through severe reduction.

1.6.1 Hydrogen treatment and UV irradiation

In 2002 Hayashi et al. [18] found that $Ca_{12}Al_7O_{33}$ can be converted to a persistent electronic conductor by heat treating the material in hydrogen environment, $Ca_{12}Al_{14}O_{33}$:H, and subsequently irradiating with UV light. At high temperatures in a hydrogen atmosphere, the formation of hydrides anions (H^-) can be represented by the equation below:

$$O^{2-} + H^{2-} \rightarrow OH^- + H^- \qquad (2)$$

The hydride anions are clathrated in the cage in place of the free O^{2-} ion; and the unit cell shows two cages occupied by H^- and two cages occupied by OH^- with the remaining eight cages unoccupied. The material shows no apparent changes in its optical or electrical property with the hydrogen treatment. The clathrated anions are ionized to a pair of OH and electron (e^-) by ultra violet irradiation. The released electron, as suggested by Hayashi et al. [18], is trapped in the cage and behaves like an F-center; which can hop under electric field, showing electrical conductivity up to 0.3 S/cm. The UV induces two optical absorption bands causing a color change from white to green, as well as an increase in conductivity. Further studies with proton

implantation showed that conductivities of 10 S/cm could be achieved and that conductivities of 0.5 S/cm remain even at 600°C [19].

1.6.2 Reduction by a base metal

The reduction of mayenite is achieved by the extraction of free oxygen ions (O^{2-}) by a base metal such as calcium leading to oxide formation. This practice was first performed by Matsuishi, et al. in 2003 [12] after realizing that it would be difficult to replace the O^{2-} species stoichiometrically by the process of hydrogen treatment. They reported the properties of the compound $[Ca_{24}Al_{28}O_{64}]^{4+}$ $(4e^-)$ synthesized by large single crystals. The samples were sealed together with metal calcium shots in silica glass tubes under vacuum and heated at 700^{o}C for various times. After the reactions they observed that the surfaces of the samples were covered with a crystalline CaO layer which was mechanically removed by polishing. There was no apparent change in the basic structure of the lattice framework, but the sample color changed from colorless to green and to black, with increasing exposure time to the calcium. The absorption edge shifted from ~5eV to ~4eV and also two absorption bands were induced at 2.8eV and 0.4eV. The shape and peak position of the two bands were found to agree exactly with those observed in the H-treated UV-irradiated mayenite, indicating that the F-like center is responsible for the induced optical absorption bands in both H-treated and Ca-treated mayenites. The injected electrons are captured by the positively charged cages and behave like an anion with spherical 1s wave function of an F-like center; they migrate throughout the crystal as polaron, which thereby enhances electronic conductivity up to ~100 S/cm at 300 K [12].

1.7 Reported electrical and optical properties

Base mayenite is an insulating material with a band gap of 4.8eV. Using Pt electrodes in a four-probe configuration to examine the electrical properties of mayenite samples Matsuishi et al. [12] reported an electrical conductivity of up to 0.3 S/cm on H-doped UV-irradiated mayenite, while mayenite with proton implantation showed conductivities of 10 S/cm could be achieved and that conductivities of 0.5 S/cm remain when measured at 600^{o}C. At room temperature, the as-grown sample has conductivity lower than the detection limit (10^{-10} S/cm), but showed conductivity of 10^{-3} S/cm after four hours of Ca treatment. Further extension of the Ca treatment duration increases the conductivity until after 1 to 2 weeks when the conductivity reaches a saturation

level (100 S/cm). Table 2 summarizes the transport properties of the Ca-reduced mayenite reported by this Matsuishi et al. [12].

The carrier content was measured using Electron Paramagnetic Resonance (EPR), but based on the absorption coefficients they found a maximum carrier concentration of $2x10^{21}$ cm^{-3} for the 240 hour sample with a mobility of ~$0.1cm^2$/V-S.

Figure 7 shows the temperature dependence of electrical conductivity (σ) measured by Matsuishi et al. [12] for low conductive samples Ca-treated for 4 hours (**b**) and 12 hours (**c**), log σ is proportional to T^{-1}. The activation energies calculated from the slopes are 130 and 160 meV, respectively. For samples Ca-treated for 18 hours (**d**) and 40 hours (**e**) the log σ is proportional not to T^{-1} but to $T^{-1/4}$ over a wide temperature range, 50 to 300K. For the highly conductive sample Ca-treated for 240 hours (**f**), log σ is almost constant and insensitive to temperature in this region.

In 2002, Hayashi et al. [18] reported on the light induced conversion of insulating mayenite to a persistent electronic conductor. They worked on hydrogen-treated polycrystalline and single crystal samples of mayenite ($Ca_{12}Al_{14}O_{33}$:H). Upon UV irradiation, two optical absorption bands were observed centered at 2.8eV and 0.4eV for the polycrystalline and single crystal sample, respectively, and remained unchanged even after the irradiation was stopped. The band gave rise to color change in the samples (colorless to yellowish green) and a drastic increase in conductivity was observed with the photon irradiation.

The conductivity of the single crystal was measured by complex impedance spectroscopy using In-Ga alloy electrodes, the value increased from less than 10^{-10} S/cm to 0.3 S/cm. With increase in the photon dose, conductivity increases and the intensity of the absorption bands become stronger as shown in Figure 8. Hayashi et al. [18] observed that the conductivity decreased from 0.3 to 10^{-7}S/cm as temperature was lowered from room temperature (300K) to 10K; and log σ was proportional to $T^{-1/4}$ not T^{-1} over the temperature range from 50 to 300K. The induced

conductive state remains unchanged even after the illumination stopped. At above 550°C H_2 gas is released from the sample and the photosensitivity is lost.

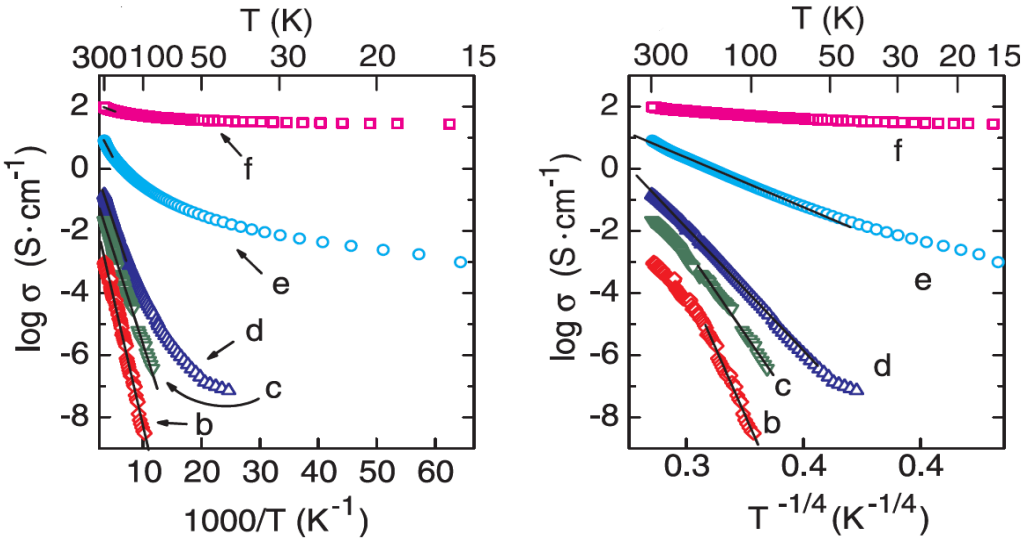

Figure 7. Temperature dependence of electrical conductivity in mayenite (T = 15 to 300 K) [12].

Table 2. Reported electrical properties of $[Ca_{24}Al_{28}O_{62}]^{+4}+4e^-$, $(0 \leq x \leq 1)$.

$[Ca_{24}Al_{28}O_{62}]^{+4}$ + $(2-x)O^{2-}+(2x)e^-$ (treatment time, h)	Conductivity at 300 K (S/cm)	Color	Carrier Content (from EPR) (cm^{-3})	SeebeckCoefficient at 300 K (μV/K)
4	$8.73x10^{-4}$	Yellowish	$7.22x10^{16}$	-780
12	$2.20x10^{-2}$	Green	$1.29x10^{18}$	-540
18	0.15	Green	$4.53x10^{18}$	-420
40	8.16	Black	$1.82x10^{19}$	-109
240	97.77	Black	$5.11x10^{19}$	-44.6

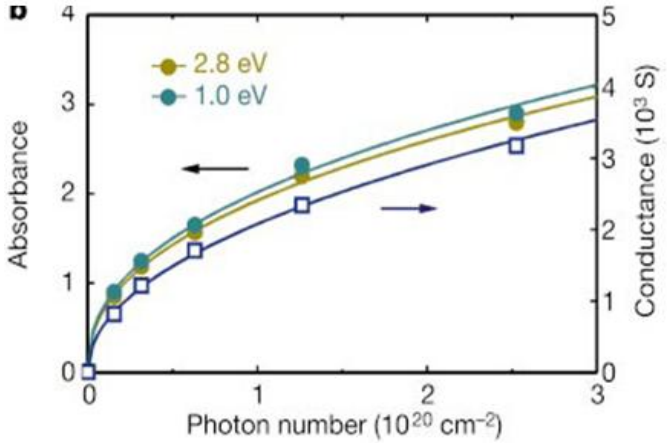

Figure 8. Dependence of conductance and absorption on photon dose [18].

Miyakawa et al. [19] worked on ion implantation of thin film samples and found that at 600˚C films bombarded with a fluence of 1.10^{18} cm^{-2} produced a conductivity of 10 S/cm, with optical transmission greater than 85% and mobility of about 0.1 cm^2/V/S. Table 3 gives a summary of the transport properties of base mayenite, hydrogen doped, H^+ implanted, and thin film mayenite.

Table 3. Reported electrical properties of $Ca_{12}Al_{14}O_{33}$ prepared by various methods.

Sample	Conductivity at 300 K (S/cm)	Absorption band (eV)	Color	Carrier Content (cm−3)	Seebeck Coefficient at 300 K (mV/K)
As prepared $Ca_{12}Al_{14}O_{33}$	$< 10^{-10}$	~ 5	colorless		
$Ca_{12}Al_{14}O_{33}$: H-treated	$< 10^{-10}$	~ 4	colorless		
Single crystal $Ca_{12}Al_{14}O_{33}$:H-treated :UV-irradiated	0.3	2.8 0.4	Green	$2\cdot 10^{19}$	-360
Thin film $Ca_{12}Al_{14}O_{33}$: H-treated : UV-irradiated	0.62 1.1	2.9 0.37	colorless		
Single crystal $Ca_{12}Al_{14}O_{33}$: H^+- implant : UV-irradiated	10	2.8 0.44	colorless	$7.6\cdot 10^{20}$	

Toda et al. [20] first demonstrated a transparent conductive thin film of mayenite in which conductive areas were patterned by light. Using polycrystalline thin films of $Ca_{12}Al_{14}O_{33}$ grown by pulsed laser deposition on various oxide substrates (e.g. MgO, SiO_2), they observed excellent optical transmission of greater than 85% in the visible range and almost 100% in the near IR range. It was observed that transmittance in the near IR region was reduced by UV irradiation due to the appearance of an optical absorption band centered at 0.4eV. The band has been associated with the F-like center formed by a localized electron released by photo-excitation in the crystallographic cage. However, the loss in the visible region is negligible in thin films. The electrical conductivity after UV irradiation increased from 10^{-10} to 0.62 S/cm; the temperature dependence and conversion from insulator to conductor of conductivity of the thin film are similar to that of single crystal mayenite.

1.8 Doped mayenite

The detailed knowledge of the transport mechanism obtained for H-doped UV-activated mayenite predicts the strong dependence of the light-induced conductivity on the atoms participating in the hopping as well as on their spatial arrangement and hence the possibility of varying the conductivity by proper doping [21]. Various dopants have been employed in order to improve on the electrical conductivity of mayenite; some of the elements tried were Mg, N, Si, Fe, Ti, etc.

1.8.1 Mg-doped mayenite ($Ca_{12-x}Mg_xAl_{14}O_{33}$)

Bertoni [3] worked on Mg-doped mayenite or $Ca_{12-x}Mg_xAl_{14}O_{33}$ where x = 0.1, 0.3, 0.5, 0.8, and 1.0. Bulk samples were prepared by solid state synthesis followed by hydrogen doping and subsequent UV irradiation. Phase purity was confirmed for each sample, matching the corresponding Powder Diffraction File (PDF) card for mayenite; however a trial with x = 1.5 resulted in a sample containing the additional phases of $CaAl_2O_4$ and MgO. For the single phase Mg-doped mayenite samples, there was not a significant change in the lattice parameters due to the small level of substitution level despite the Mg^{2+} ion (0.72 Å for CN = 6) being significantly smaller than the Ca^{2+} ion (1.0 Å for CN = 6). Figure 9 shows X-ray powder diffraction patterns of the Mg-doped samples compared to pure mayenite. No structural changes in hydrogen-doped

and hydrogen-doped/UV irradiated samples were observed when compared to the pattern of the pure mayenite.

The conductivity of the samples was measured using Impedance Spectroscopy (IS) and Figure 10 shows the conductivity of as-prepared Mg-substituted samples (x = 0.3 and 1.0) compared to pure mayenite and yttria-stabilized zirconia (YSZ). $Ca_{12}Al_{14}O_{33}$ shows a conductivity of about 10 times less than that of YSZ and the $Ca_{12-x}Mg_xAl_{14}O_{33}$ samples show even lower conductivities, about 20 times less than YSZ for x=0.3 and 45 times less than YSZ for x=1.0.

Introduction of Mg in the sample increases the activation energy for the diffusion of the carriers in the bulk sample, indicating that the more Mg the higher the concentration of less mobile carries e.g. O^{2-}, OH^-, since magnesium is known to favor the formation of less mobile oxygenous species [3]. However, it has been reported that this does not affect the behavior of the samples after the hydrogen/UV treatment because hydrogen is still incorporated into samples through an exchange reaction between O^-_2 and H^- and/or between O_2^{-2} and $2H^-$.

Conductivity was found to be strongly dependent on the level of Mg substitution and also on temperature. Figure 11 shows the temperature dependence of the conductivity for the hydrogen/UV treated Mg-substituted samples, with an error of approximately 10% due to uncertainty in geometric factors. Between room temperature and about 130^{o}C, the conductivity rises reversibly with increasing temperature; but as the temperature exceeds 135^{o}C, the conductivity begins to drop irreversibly. The temperature dependence of the conductivity of these doped samples was observed to be similar to that of a pure mayenite (shown in Figure 10). The drop in conductivity is a result of the release of hydrogen as the temperature exceeds the decomposition temperature.

Compared to pure mayenite, there is a slight shift to higher values in decomposition temperature with increased substitution level. From a comparison of the total energies of the 12 fully relaxed cages with different Mg site locations, it was found that the H^- relaxes toward the Mg atom and

demonstrates a strong Mg-H bonding; this fact, combined with the tendency for Mg atoms to cluster, could account for the sluggish decomposition kinetics in the Mg-substituted samples [3].

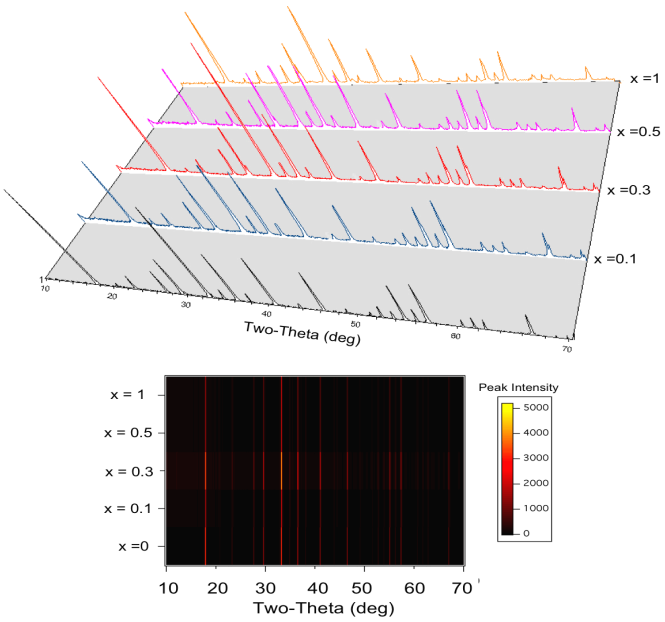

Figure 9. Two views of X-ray powder diffraction patterns of $Ca_{12-x}Mg_xAl_{14}O_{33}$ (x =0.1, 0.3, 0.5, 1) [3].

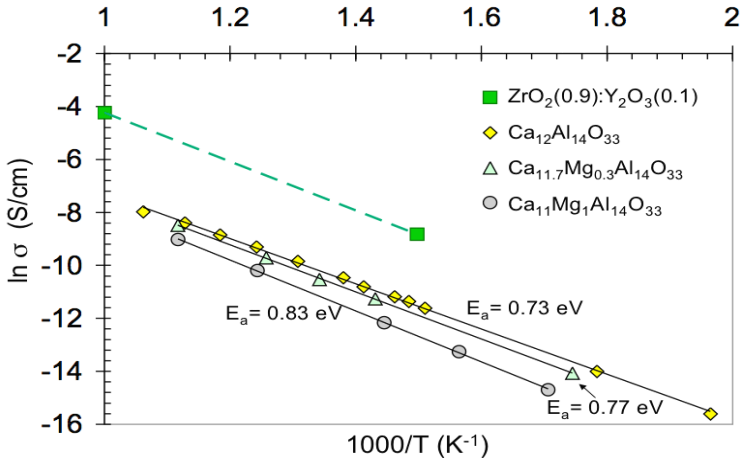

Figure 10. Comparision of the ionic conductivity for pure $Ca_{12}Al_{14}O_{33}$, along with two samples of Mg doped mayenite, and YSZ [3].

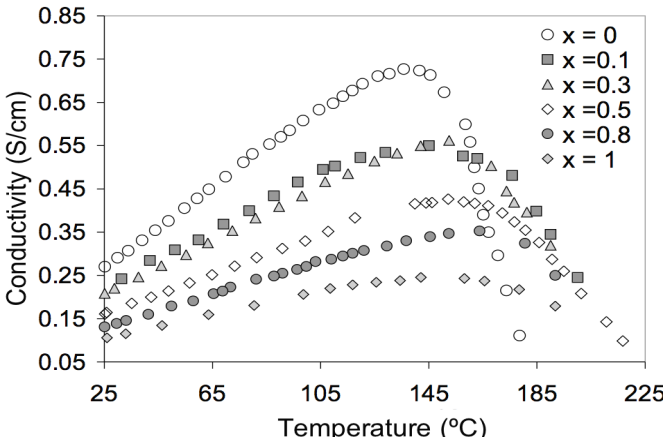

Figure 11. Temperature dependence of the conductivity for UV illuminated/H-doped $Ca_{12-x}Mg_xAl_{14}O_{33}$ (x = 0, 0.1, 0.3, 0.5, 0.8, 1) pellets (25-225^{o}C).

Table 4 is a summary of the transport properties of Mg-doped mayenite at room temperature and 125^{o}C. Figure 12 is the display of the diffuse reflectance spectra of the $Ca_{12-x}Mg_xAl_{14}O_{33}$ system characterizing the optical properties. Bertoni et al. observed an increase in transmission with doping level while the energy of the optical gap remained constant (2.6eV). The increase in transmission was found to be consistent with the drop in the carrier concentration shown above.

Table 4 Transport data for $Ca_{12-x}Mg_xAl_{14}O_{33}$ at 25 and 125°C.

Substitution level (*x*)	Carrier content (cm^{-3})	Conductivity (S/cm)		Mobility (cm^{-2}/V-S)	
		25 °C	125 °C	25°C	125 °C
0.0	$1.08x10^{21}$	0.270	0.711	$1.57x10^{-3}$	$4.12x10^{-3}$
0.1	$6.43x10^{20}$	0.242	0.534	$2.35x10^{-3}$	$5.18x10^{-3}$
0.3	$5.94x10^{20}$	0.209	0.515	$2.19x10^{-3}$	$5.41x10^{-3}$
0.5	$4.72x10^{20}$	0.165	0.384	$2.18x10^{-3}$	$5.07x10^{-3}$
0.8	$3.19x10^{20}$	0.131	0.318	$2.56x10^{-3}$	$6.22x10^{-3}$
1.0	$2.08x10^{20}$	0.106	0.234	$3.19x10^{-3}$	$7.04x10^{-3}$

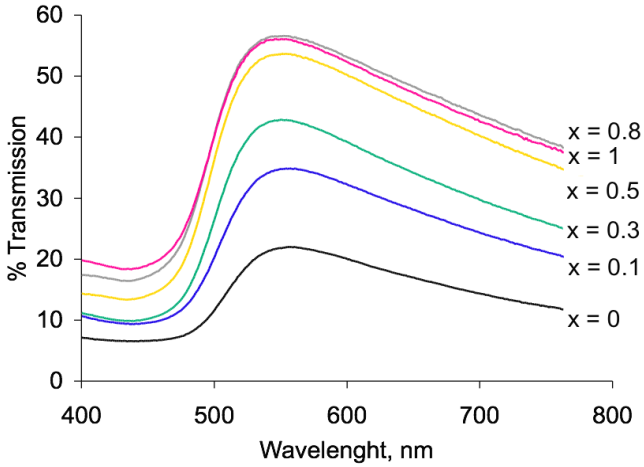

Figure 12. Optical properties of $Ca_{12-x}Mg_xAl_{14}O_{33}$ [3].

1.8.2 Si-doped mayenite ($Ca_{12}Al_{14-x}Si_xO_{33+x/2}$)

Bertoni [3] also studied Si-doped mayenite. The Si-substituted samples were prepared by hydrothermal synthesis a technique used in synthesizing phases not easily formed by solid state reaction that involves lower temperatures due to the addition of pressure as a parameter. This applies to Si substituted mayenite ($Ca_{12}Al_{14-x}Si_xO_{33+x/2}$) when trying to achieve substitution levels falling outside the equilibrium composition [22]. The prepared samples were hydrogen-treated in a high temperature furnace but due to the instability of the samples, they decomposed into the equilibrium oxides. Therefore, ion implantation, carried out at 300^{o}C to avoid decomposition, was used to incorporate a sufficient amount of hydrogen and was followed by subsequent UV irradiation.

The powders of the as-prepared samples were characterized using X-ray powder diffraction and the resulting diffraction patterns showed the presence of mayenite and lime (CaO). Bertoni [3] was not able to eliminate the CaO phase during preparation due to the meta-stability of the $Ca_{12}Al_{14-x}Si_xO_{33+x/2}$ phase once the Si was added. Figure 13 shows the changes in relative intensities for the CaO and mayenite peaks for the varying amounts of Si additions. They reported a consistent decrease in intensity of the CaO I/I_0 = 100% reflection with an increase in substitution level and a gradual shift of the mayenite peaks to higher angles. The shift was due to Si^{4+} smaller ionic radius (0.26 Å for CN = 4) compared to Al^{3+} (0.39 Å for CN = 4).

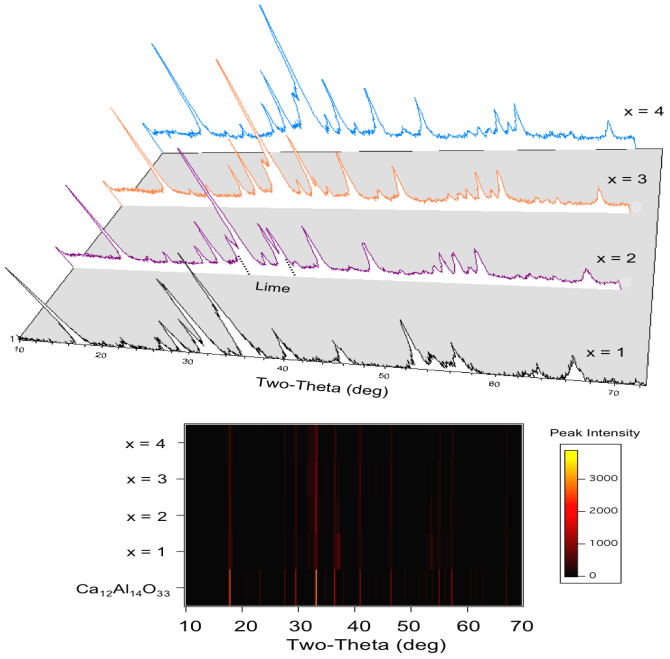

Figure 13. Two views of X-ray diffraction data of $Ca_{12}Al_{14-x}Si_xO_{33+x2}$ (x= 1, 2, 3, 4) [3].

The plot of the lattice parameters, obtained by Rietvield refinement, versus Si content is shown in Figure 14. Phase analysis of the ion implantated/UV irradiated samples showed no evident structural change when compared to the as-prepared specimens. The observed electrical conductivity of the Si-doped mayenite samples was two or three times that of the pure mayenite, 0.25 S/cm for x = 2 and 0.61 S/cm for x = 4. With the substitution of Al^{3+} with Si^{4+}, and a decrease in the fraction of occupied sites, the unit cell had to accommodate more free oxygen anions to balance the framework allowing for more hydrogen to be incorporated into the sample and correspondingly more electrons should be released after UV irradiation [3].

This was believed to cause the increase in conductivity; increase in the electron population in the doped samples increased the number of hopping centers, thereby increasing conductivity even with a slight decrease in the fraction of occupied sites. The temperature dependence of the conductivity for the hydrogen ion-implanted/UV irradiated Si-doped samples is shown in Figure 15. The measurements were collected between room temperature and 100^{o}C to avoid phase decomposition of the samples. At room temperature the pure mayenite showed a conductivity of 0.15 S/cm while that of the Si-substituted sample (x = 4) was 0.61 S/cm. These values are

relatively low and might have resulted from low hydrogen incorporation into the samples at low implantation temperature (300^{o}C).

Table 5 summarizes the conductivity results obtained for the $Ca_{12}Al_{14-x}Si_xO_{33+x/2}$ phase at room temperature. The conductivity measurement for the sample $Ca_{12}Al_{13}Si_1O_{33.5}$ (x = 1) was difficult to obtain probably due to the high amount of the insulating CaO phase in the sample. It is important to mention that the lime content in the other Si-substituted samples, even though small, may be playing a role in increasing the Seebeck coefficients [3].

The optical properties were found to be consistent with the electrical results, with an increase in Si content correlating to an increase in carrier concentration, the transmission goes down. Bertoni [3] reported a remarkable correlation between all experimental results with theoretical calculations and suggests that due to probable hopping paths and the number of available sites for hopping, the calculations were complicated and the estimation of the carrier content and mobility is impossible.

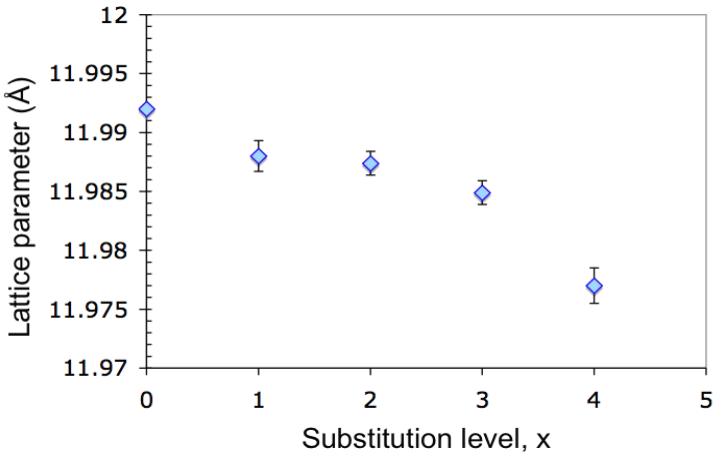

Figure 14. Lattice parameter versus substitution level of $Ca_{12}Al_{14-x}Si_xO_{33+x/2}$ (x = 0, 1, 2, 3, 4) [3].

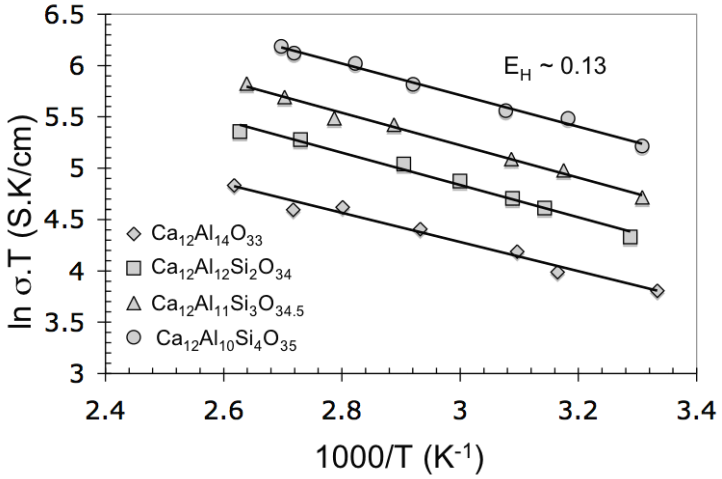

Figure 15. Conductivity versus temperature for UV-irradiated/proton implanted $Ca_{12}Al_{14-x}Si_xO_{33+x/2}$ (x =0, 2, 3, 4) [3].

Figure 16 shows the diffuse reflectance plots of ion-implanted/UV irradiated $Ca_{12}Al_{10}Si_4O_{35}$ phase compared to ion-implanted/UV irradiated $Ca_{12}Al_{14}O_{33}$. The two samples showed high transparency before activation, about 95% transmission in the visible spectrum, with band gap energies of 4.43eV and 4.76eV for the pure and Si-doped samples, respectively. However, after activation the transmission dropped to 65% and 53% for the pure and doped sample respectively. The results are consistent with the higher carrier content of the Si- substituted sample [3].

Table 5. Conductivity of UV-irradiated proton implanted $Ca_{12}Al_{14}O_{33}$ and $Ca_{12}Al_{14-x}Si_xO_{33+x/2}$

Substitution Level (x)	Conductivity (RT) (S/cm)
0	0.15
2	0.25
3	0.37
4	0.61

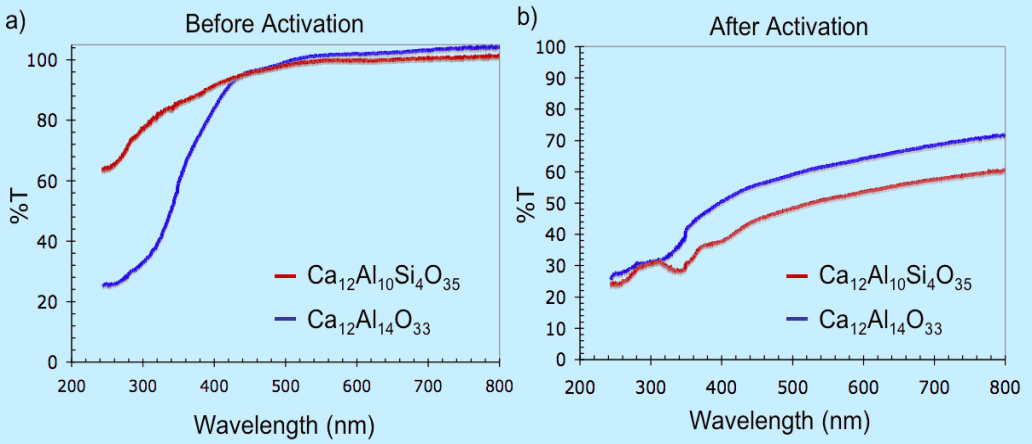

Figure 16. Diffuse reflectance of UV-irradiated proton implanted $Ca_{12}Al_{10}Si_4O_{35}$ compared to $Ca_{12}Al_{14}O_{33}$ [3].

1.8.3 Fe-doped Mayenite ($Ca_{12}Al_{14-x}Fe_xO_{33}$)

Boysen et al. [23] investigated the structure and properties Fe-doped mayenite ($Ca_{12}Al_{14-x}Fe_xO_{33}$) using neutron and synchrotron powder diffraction. The samples were dopes with 0.1 and 2.5 mol% Fe, and were synthesized via sol-gel process. The data collected were analyzed by the Rietveld method, including an-harmonic Debye-Waller factors to describe the atomic displacement parameters, and by using difference Fourier maps. The phase analysis revealed that when x = 2.5 10 wt% $CaAl_2O_4$ appeared as a secondary phase and a stoichiometric composition of $Ca_{12}Al_{13.75}Fe_{0.25}O_{32}O_1$ was obtained showing no appreciable amounts of additional species like OH^- or O^{-2}.

They reported that the stoichiometric site occupancy does not change with temperature, but noted that there seemed to be some reduction at 700°C and a very large uncertainty at 900°C. The temperature dependence of the refined site occupancy is shown in Figure 17; the horizontal line depicts site occupancy for ideal stoichiometric composition.

Figure 18 is a plot of the temperature dependence of the isotropic atomic displacement parameters (U_{iso}) for the sample. The U_{iso}, corresponding to root mean square (rms) amplitudes, can become exceptionally large at high temperatures indicating extreme disorder of the encaged

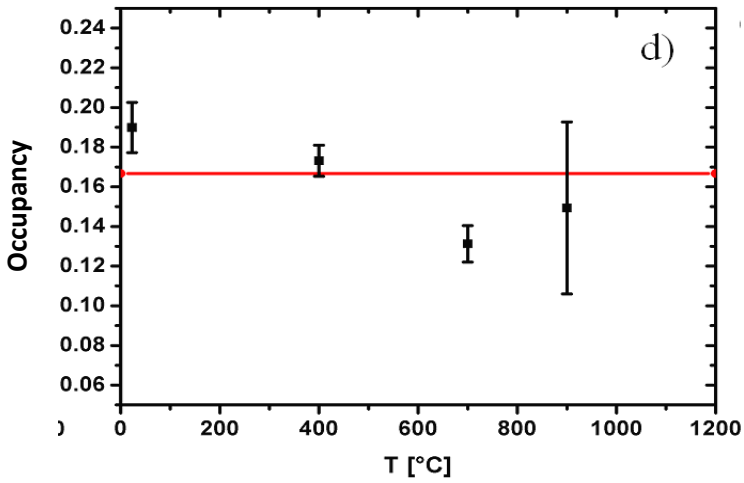

Figure 17. Temperature dependence of occupancy for Fe-mayenite [23].

species possibly related to their diffusion properties [24]. Similar to site occupancy factor refined from the 900^{o}C data show in Figure 17, Figure 18 shows an extremely uncertainty for the U_{iso} refined from the 900^{o}C data for Fe-mayenite. The group also studied high temperature difference Fourier plots to give more insight into the diffusion properties of this sample. They reported no unambiguous residual density in the sample (Figure 19), which might explain the large uncertainties for the corresponding site occupancy and atomic displacement parameters refined from the 900^{o}C data [25].

The Figure 19 shows that O electron density is considerably smeared out at room temperature (a) but not detectable above 900^{o}C (b), which corroborates with the unrealistic large U_{iso} and the large uncertainities on the refined site occupancy.

The determination of the diffusion path is prohibited by the extremely low local densities. They suggested that the invisibility of any oxygen density within the cage may have resulted from even more extreme delocalization, that is, extremely high diffusion, or from a loss of oxygen in conjunction with Fe reduction [23].

The Fe mayenite was found to show large disorder at room temperature and extreme delocalization at high temperatures suggesting high anionic conductivity [25] but the authors suggested that more work is needed to verify these suggestions.

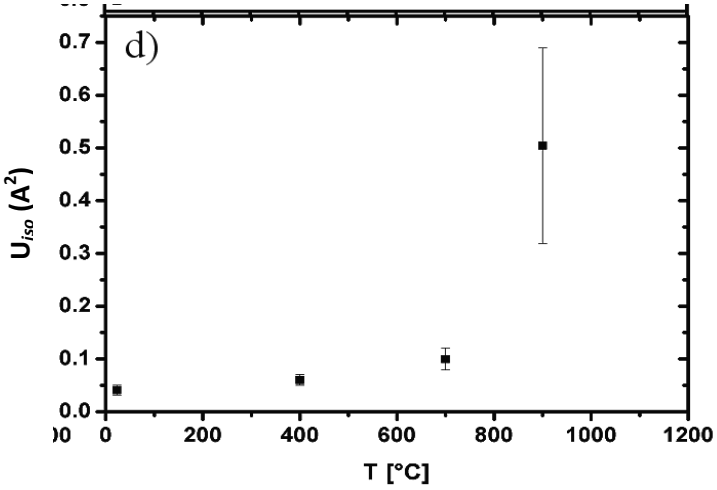

Figure 18. Temperature dependence of isotropic displacement parameters of encaged anions for Fe-mayenite [24].

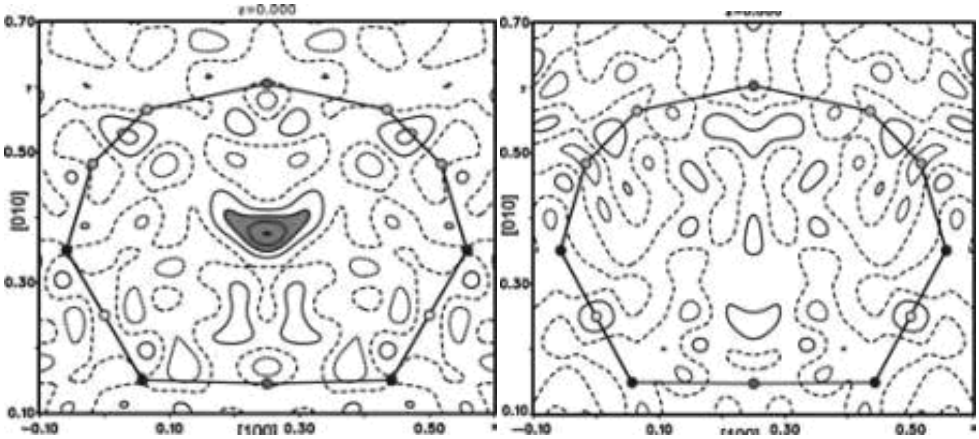

(a) **(b)**

Figure 19. Difference Fourier maps of Fe-mayenite at (a) room temperature and (b) 1050 °C, after refinement with empty cage [25].

1.9 $CaO-Al_2O_3-Fe_2O_3$ system

Dayal et al. [26] studied the phase relations in the $CaO-Al_2O_3-Fe_2O_3$ ternary system using the standard quenching techniques; the calcium aluminate$12CaO.7Al_2O_3$ was encountered as a primary phase at liquidus temperatures. The solid phase forms a range of solid solution of which the mechanism is $Fe^{3+}\leftrightarrow Al^{3+}$ replacement. Figure 20 is a ternary phase diagram of $CaO-Al_2O_3-Fe_2O_3$ system showing all the primary phase. The system has some meta-stable phases that are not shown in the diagram.

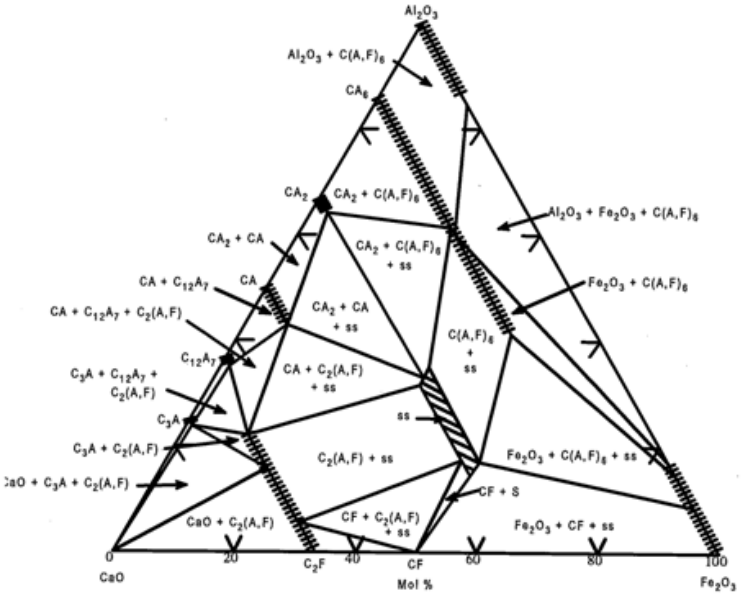

Figure 20. $CaO-Al_2O_3-Fe_2O_3$ ternary phase diagram (PDFC # 02492, volume 02).

CHAPTER 2

METHODOLOGY AND EXPERIMENTAL

2.1 Synthesis of mayenite

2.1.1 Solid state process

Solid state reactions are commonly used in synthesis of ceramic powders, involving the direct combination of two or more powdered solids at high temperature. This technique usually involves an initial lower temperature firing or calcination step where CO_2 is driven off when starting with a carbonate form. Subsequent higher temperature firings involve chemical reactions between the starting materials to form new phase. This type of synthesis is common for the production of complex oxides like titanates, ferrites and silicates [27]. Solid state synthesis has been previously used to prepare bulk samples of mayenite and most of the reported physical properties of mayenite have been obtained on samples synthesized using this technique.

2.1.2 Sol-gel process

Sol-gel synthesis is often used in preparing thin films and involves the conversion of a solution of molecular precursors by a chemical reaction into a sol or a gel, which is subsequently transformed into a crystalline material upon drying and subsequently firing [28]. Synthesis steps are performed under ambient conditions, involving no difficult technical challenges in terms of instrumentation or special environment. The process is regarded as a cost-effective and simple technique that can easily lead to the formation of uniform thin films since the precursors are mixed in solution and can interact more easily [29].

Samples produced by sol-gel usually do not require as high a firing temperature compared to those synthesized via conventional solid state synthesis. This makes the sol-gel technique viable for making samples that are unstable and decompose at high temperatures.

2.2 Experimental details

Samples of pure ($Ca_{12}Al_{14}O_{33}$) and Fe doped ($Ca_{12}Al_{14-x}Fe_xO_{33}$) mayenite were produced by both solid state and sol-gel syntheses. Five samples were prepared using solid state synthesis with varying Fe concentration where x = 0, 0.05, 0.1, 0.25 and 0.3; two sets of samples were made via the sol-gel technique, the first set was prepared with varying Fe concentrations where x = 0, 0.05, 0.1, 0.2, 0.3 and 0.4, the second set of four samples did not contain Fe (x = 0) and were synthesized for studying the firing temperature.

2.2.1 Solid State Synthesis

For the solid state synthesis, starting powders of $CaCO_3$, Al_2O_3, and Fe_2O_3 were used. After calculating and weighing out the appropriate proportions of the powders, they were mixed using an agate mortar and pestle with methanol to make a slurry. The slurry was left to dry and subsequently the powder was pressed into pellets using a hydraulic press. The samples were first fired in the furnace at 1200^oC for 16 hours, then re-ground with agate mortar and pestle and re-pressed into pellets. The base mayenite sample was subsequently fired at 1350^oC for 23.5 hours, while the Fe doped samples were fired at 1350^oC for 18 hours; the samples were all air quenched.

2.2.2 Sol-gel Synthesis

The starting materials for the samples synthesized using the sol-gel technique included $Ca(NO_3)_2 \bullet 4H_2O$, $Al(NO_3)_3 \bullet 9H_2O$, $Fe(NO_3)_3 \bullet 9H_2O$, and citric acid ($C_6H_8O_7$) as organic fuel. Appropriate amounts of nitrates were measured and mixed in a beaker with de-ionized water; the mixture was heated on a hot plate up to 60^oC before pouring in the citric acid. The citrate-nitrate mixture was heated and vigorously stirred with magnetic agitator at 90^oC until a gel was formed (about 7 hours). Figure 21 shows the laboratory set-up under the fume hood. The resulting gel was placed in a drying oven at 130°C where auto-combustion occurred and the gel transformed

into a cake-like structure, which was subsequently crushed into powder using the agate mortar and pestle. The resulting powders were pressed into pellets; the first set of samples were fired in the furnace at 1000^{o}C for 4 hours while the second set of samples were each fired at different temperatures (T = 1100, 1000, 900 and 800˚C) for four hours. All samples were quenched in air. All the synthesized samples from both methods are shown in table 6.

Table 6. Summary of all the samples prepared using solid state and sol-gel synthesis.

Fe concentration (x)	Technique	Temperature (˚C)	Firing time (hr)
0.00	Sol-gel	1100	3.5
	Sol-gel	1000	4
	Sol-gel	900	4
	Sol-gel	800	4
	Solid state	1350	23.5
0.05	Sol-gel	1000	4
	Solid state	1350	18
0.10	Sol-gel	1000	4
	Solid state	1350	18
0.20	Sol-gel	1000	4
0.25	Solid state	1350	18
0.30	Sol-gel	1000	4
	Solid state	1350	18
0.40	Sol-gel	1000	4

Figure 21. Sol-gel synthesis set up, within the hood, for mayenite production.

2.3 X-ray Powder Diffraction Characterization and Data Analysis

Samples were ground and X-ray powder diffraction was used iteratively to characterize the samples. If enough powder was available data were collected using back loaded deep welled sample holders. If there was a limited amount of powder the data were collected by dispersing the powder with methanol on a Si zero background plate. During the data collection the samples were spinning to improve sampling statistics. The data were collected on a PANalytical X'Pert PRO MPD θ-θ diffractometer. The diffractometer was equipped with an X'celerator Real Time Multiple Strip (RTMS) detector that allows ultrafast data collection. Data were collected using Cu Kα radiation and the system was operated at 45KV and 40mA. The data were collected over a 2θ range of 5˚-140˚ with a count time set so that each data collection lasted approximately 20 minutes. In several instances data were collected using a longer count times.

X-ray powder diffraction data were analyzed using either Jade or HighScore plus to identify the phases present, and Rietveld refinements were performed using the EXPGUI graphical interface [30] for the General Structure Analysis System (GSAS) [31]. Rietveld refinements compare

observed X-ray powder diffraction data to a calculated model. From the collected data a statistically expected R value, R_{exp}, can be calculated and from the least squares refinement a weighted profile R, R_{wp}.is obtained. The goodness-of-fit, χ^2 is the ratio between R_{wp} and R_{exp} and for a good guideline is that it should be between 1 and 1.5, however, if the Rexp is low a good fit can be obtained resulting in a considerably higher χ^2. It should be emphasized that in addition to the χ^2 as a indicator of the quality of the refinement, visual inspection of the comparison of the observed data and the calculated pattern is necessary.

CHAPTER 3
RESULTS AND DISCUSSIONS

3.1 Physical Property Observations

As expected, the size of the pellets was reduced after firing with significantly more reduction occurring for the samples synthesized using the sol-gel technique, which often shrunk to approximately one third of their original size. In part, this is due to the loss of gaseous compounds like NO_2, CO_2, NO, etc.

The samples changed colors upon firing. The sol-gel samples prepared for studying the effects of increasing Fe content were originally cream colored powders that turned white; the white color changed into light green with Fe incorporation and got darker as the Fe content increases. The sol-gel samples prepared for studying the effects of firing temperature were all white after firing at different temperatures except for the sample fired at 800˚C which turned slightly grey. The solid state sample without Fe turned from white to light cream, while the samples containing Fe changed from a reddish color to a greenish color that became darker as the Fe content increased.

When grinding by hand the samples were observed to show variations in hardness. As expected as the temperature was increased the samples were harder to grind, in contrast to the samples being easier to grind when the Fe content was increased; these observations were more obvious in the solid state samples.

3.2 Phases Analysis

The undoped samples prepared by the sol-gel technique were all single phase except for the sample fired at 800˚C. This sample contains unreacted $CaCO_3$, and Fe_2O_3 suggesting that equilibrium was not reached at that temperature. This result suggests that the approximate minimum temperature to obtain single phase is 900˚C. Table 7 compares the phases identified for the undoped sol-gel samples fired at various temperatures.

Table 8 summarizes the identified phases in the Fe doped samples prepared by sol-gel method with varying Fe contents. Samples with x = 0, 0.05 and 0.3 were single phase, however, X-ray powder diffraction data collected on the sample with, x = 0.1 showed two extra unidentified peaks. The X-ray powder diffraction data also indicated a minor amount of the meta-stable phase $Ca_5Al_6O_{14}$ was present as a secondary phases for the samples where x = 0.2 and 0.4.

X-ray powder diffraction data collected on the samples synthesized via the solid state method showed the more secondary phases compared to samples synthesized via the sol-gel technique. Only the sample where x = 0 was single phase, all others contained secondary phases. With the exception of the sample where x = 0.3, the secondary phases were identified and are summarized in Table 9

3.3 Diffraction patterns

Figure 22 shows the X-ray powder diffraction data for the undoped sol-gel samples. As can be seen, the patterns superimpose over one another showing same diffraction pattern except for the sample fired at 800^{o}C which has multiple phases thereby exhibiting additional diffraction peaks indicative of the secondary phases summarized in Table 6. The high background displayed in this pattern could be attributed to amorphous content. The X-ray powder diffractometer was configured with a diffracted beam monochromator while collecting data on the sample fired at 1100^{o}C significantly cutting down on the intensity.

Table 7. Phases identified by X-ray powder diffraction in undoped sol-gel mayenite samples fired at different temperatures.

Temperature (˚C)	Firing Time (hr)	Phases
1100	3.5	$Ca_{12}Al_{14}O_{33}$
1000	4	$Ca_{12}Al_{14}O_{33}$
900	4	$Ca_{12}Al_{14}O_{33}$
800	4	$Ca_{12}Al_{14}O_{33}$ (64.89 wt%), $CaAlO_4$ (21.88 wt%), $CaCO_3$ (13.23 wt%)

Table 8. Phases identified by X-ray powder diffraction in Fe doped mayenite ($Ca_{12}Al_{14-x}Fe_xO_{33}$) samples prepared via sol-gel technique and fired at 1000˚C for 4 hours.

Fe content (x)	Phases
0.00	$Ca_{12}Al_{14}O_{33}$
0.05	$Ca_{12}Al_{14}O_{33}$
0.1	$Ca_{12}Al_{14}O_{33}$
0.2	$Ca_{12}Al_{14}O_{33}$ (99.92 wt%), $Ca_5Al_6O_{14}$ (0.08 wt %)
0.3	$Ca_{12}Al_{14}O_{33}$
0.4	$Ca_{12}Al_{14}O_{33}$ (97.27 wt%), $Ca_5Al_6O_{14}$ (2.73 wt%),

Tables 9. Phases identified by X-ray powder diffraction in the Fe doped mayenite ($Ca_{12}Al_{14-x}Fe_xO_{33}$) samples prepared via solid state synthesis fired at 1350˚C.

Fe content (x)	Time (hrs)	Phases
0	23.5	$Ca_{12}Al_{14}O_{33}$
0.05	18	$Ca_{12}Al_{14}O_{33}$ (99.98 wt%), $Ca_2(Al,Fe)O_5$ (0.02 wt%)
0.1	18	$Ca_{12}Al_{14}O_{33}$ (94.58 wt%), Ca_3AlO_6 (5.42 wt%)
0.25	18	$Ca_{12}Al_{14}O_{33}$ (99.55 wt%), $Ca_2(Al,Fe)O_5$ (0.45 wt%)
0.3	18	$Ca_{12}Al_{14}O_{33}$

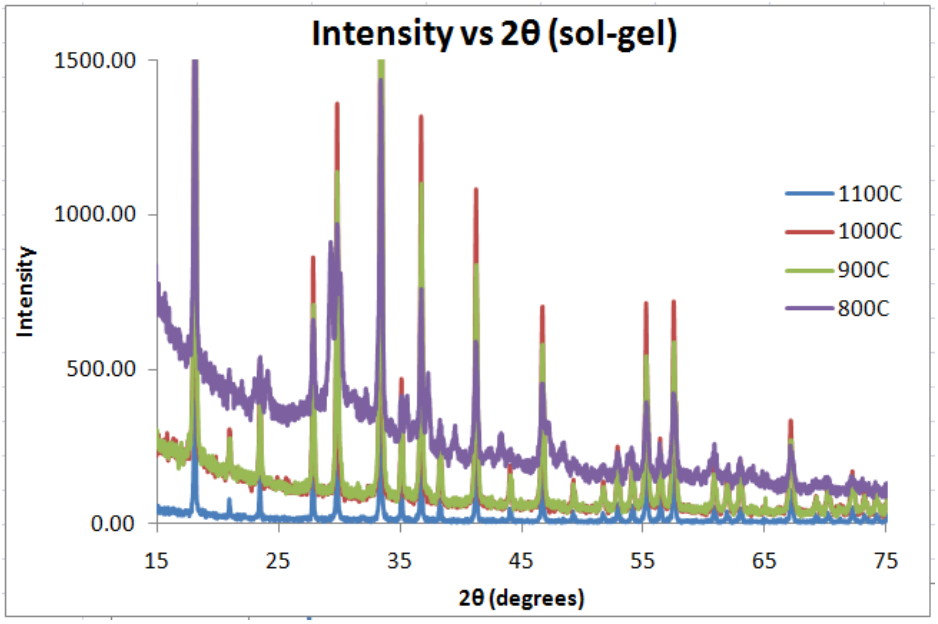

Figure 22. X-ray powder diffraction data of samples synthesized using the sol-gel technique and subsequently fired at different temperatures.

The X-ray powder diffraction patterns of the samples synthesized using the sol-gel technique with varying Fe concentrations are shown in Figure 23. Except for a few extra peaks resulting from the secondary phases present in the samples where x = 0.1, 0.2 and 0.4, the patterns are superimposed over one another. The intensities are not directly comparable due to the different instrumental optics used for collecting the data.

Figure 24 shows the X-ray powder diffraction patterns of the samples made via solid state synthesis. The patterns show mayenite as the majority phase plus a additional few peaks resulting from the secondary phases. Again, the intensities and background are different due to differences in the incident and diffracted beam optics.

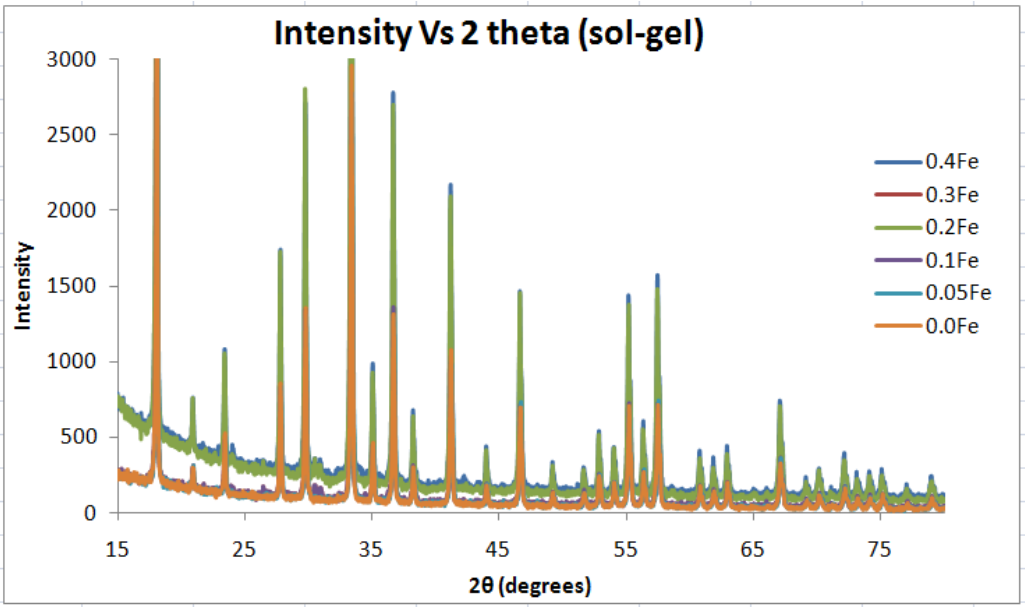

Figure 23. Powder X-ray diffraction data of samples synthesized using the sol-gel technique containing varying amounts of Fe and fired at 1000°C.

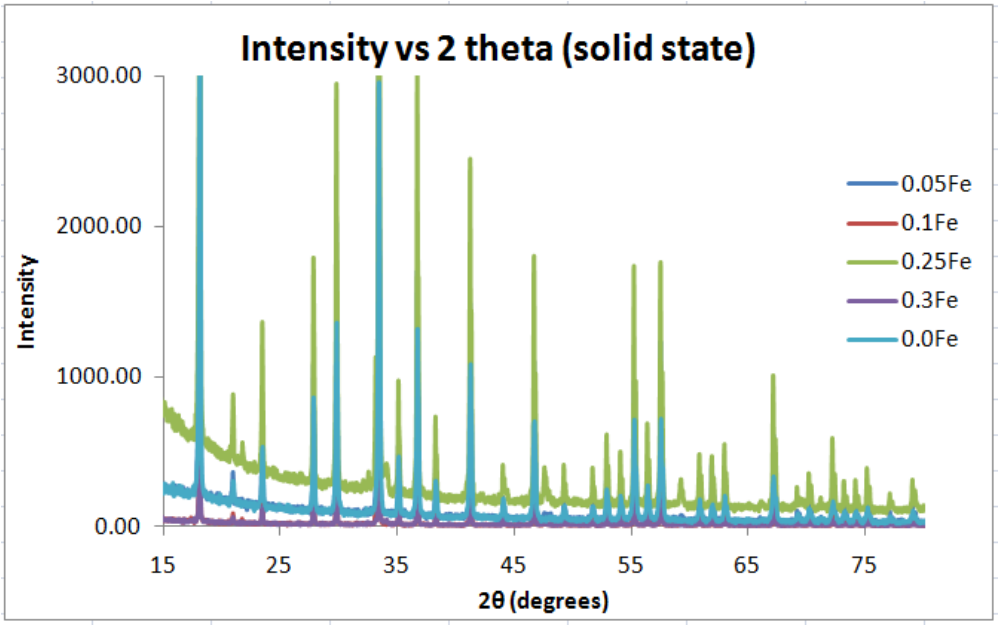

Figure 24. X-ray powder diffraction data of samples synthesized using the solid state technique with varying amounts of Fe.

3.4 Rietveld Refinement Results

Figure 25 shows the variation of the refined lattice parameters, obtained from the Rietveld refinements, as a function of Fe content for samples synthesized using the solid state technique. For all the samples the lattice parameter showed a slight increase with increasing Fe concentration. Figure 26 shows the variation of the refined lattice parameters as a function of Fe content for the samples synthesized using the sol-gel technique. The increase in lattice parameter suggests that Fe is replacing Al since Fe has larger ionic radii. Lattice parameters from the two techniques are plotted in figure 27, the parameters from the sol-gel samples showed less linearity than those of solid state.

Tables 10 and 11 summarize the refined parameters for the sol-gel samples at different temperatures, sol-gel samples with varying Fe concentrations and solid state samples with different Fe contents.

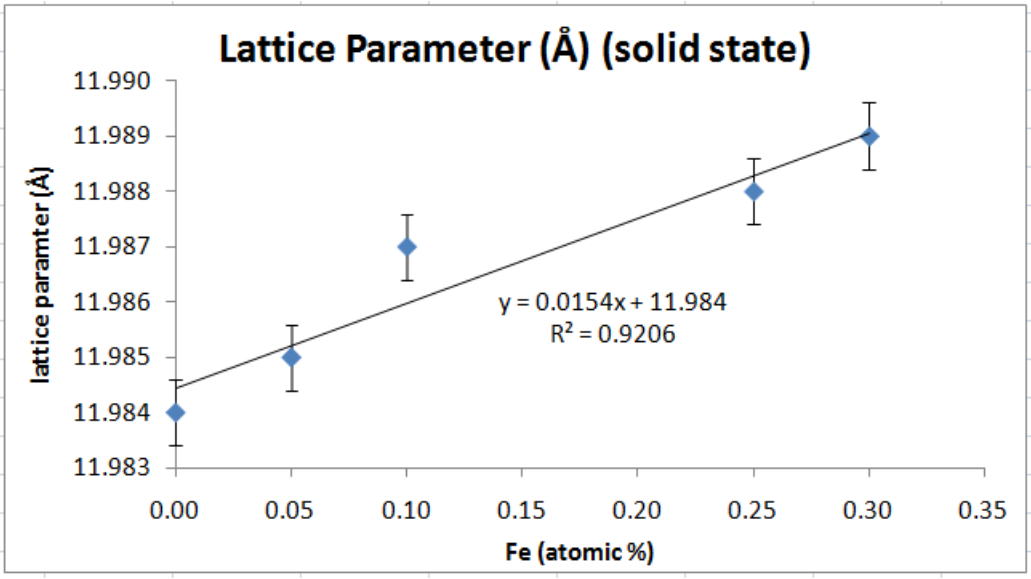

Figure 25. Graph of lattice constant versus Fe content for solid state samples.

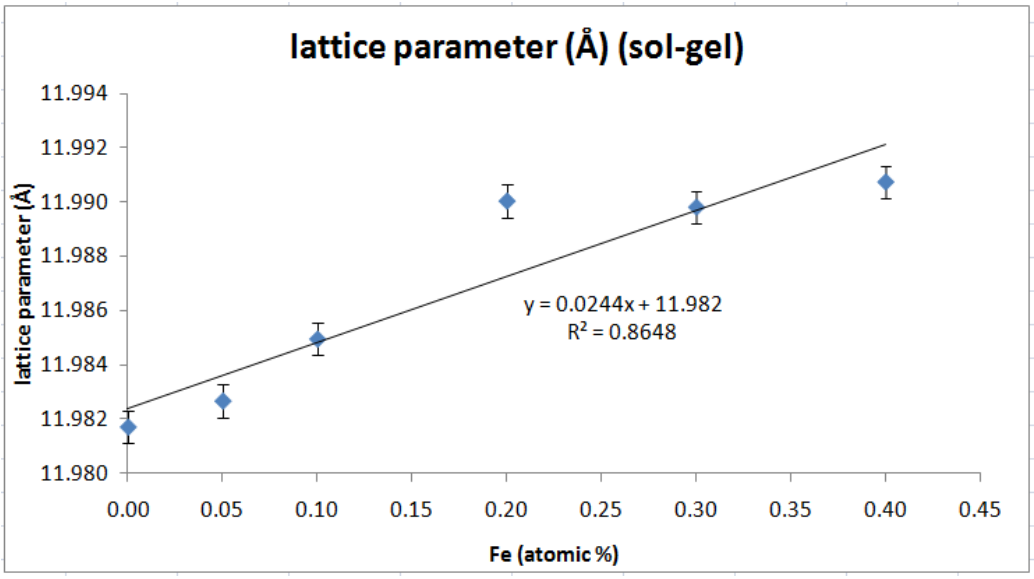

Figure 26. Plot of lattice constant versus Fe content for sol-gel samples.

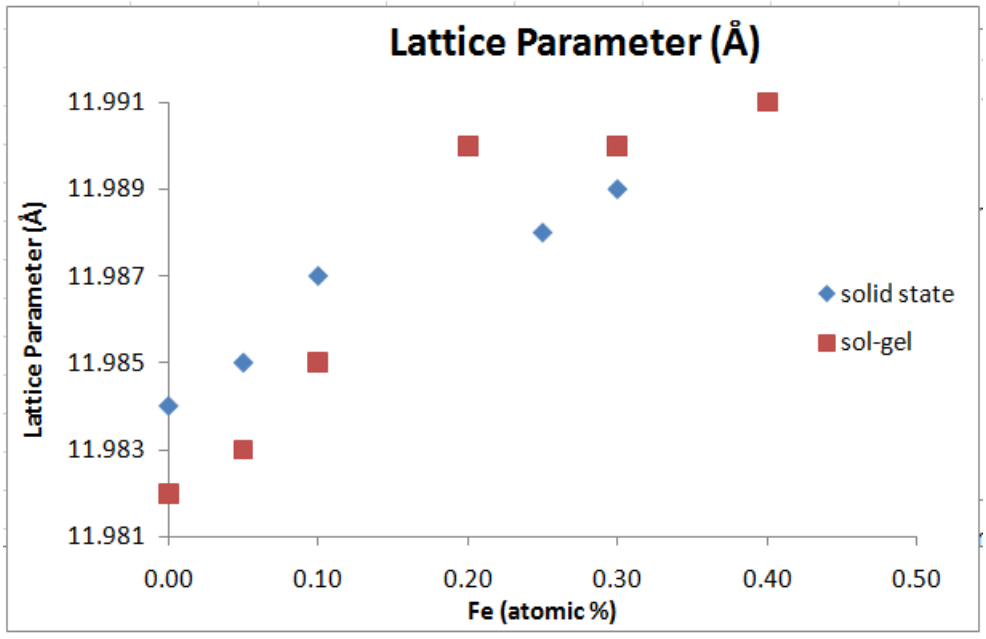

Figure 27. Plot of lattice constant versus Fe content for solid state and sol-gel samples.

Table 10. Summary of refined lattice parameters of the prepared mayenite samples.

Fe concentration (x)	Technique	Temperature (˚C)	Lattice constant (Å)
0.00	Sol-gel	1100	11.9817(2)
	Sol-gel	1000	11.9848(2)
	Sol-gel	900	11.9847(2)
	Sol-gel	800	11.989(1)
	Solid state	1350	11.9844(1)
0.05	Sol-gel	1000	11.9827(1)
	Solid state	1350	11.9851(1)
0.10	Sol-gel	1000	11.9850(1)
	Solid state	1350	11.9870(2)
0.20	Sol-gel	1000	11.9904(2)
0.25	Solid state	1350	11.9880(1)
0.30	Sol-gel	1000	11.9898(2)
	Solid state	1350	11.9890(1)
0.40	Sol-gel	1000	11.9907(1)

† The estimated standard deviations (esd) are given in ( ).

Table 11. Summary of refined fit parameters of the prepared mayenite samples.

Fe concentration (x)	Technique	Firing temperature (˚C)	R_{EXP}	W_{RP}	χ^2
0.00	Sol-gel	1100	0.2021	0.2106	1.090
	Sol-gel	1000	0.0938	0.1079	1.328
	Sol-gel	900	0.0936	0.0978	1.093
	Sol-gel	800	0.0592	0.1334	5.098
	Solid state	1350	0.0752	0.1002	1.781
0.05	Sol-gel	1000	0.0936	0.1043	1.246
	Solid state	1350	0.0924	0.1129	1.496
0.10	Sol-gel	1000	0.0579	0.0847	2.145
	Solid state	1350	0.2081	0.2246	1.171
0.20	Sol-gel	1000	0.0573	0.0912	2.555
0.25	Solid state	1350	0.0548	0.0853	2.429
0.30	Sol-gel	1000	0.0895	0.0972	1.182
	Solid state	1350	0.2102	0.2216	1.162
0.40	Sol-gel	1000	0.0552	0.0768	1.945

CONCLUSIONS

Fe was introduced into mayenite using both solid state synthesis and sol-gel synthesis. Samples prepared using sol-gel were able to incorporate more Fe while maintaining phase purity. Most of Tthe solid state samples showed multiple phases with introduction of Fe. Samples synthesized using the sol-gel technique were phase pure when fired at 900˚C or above. Sol-gel samples fired at 800˚C did not reach equilibrium and there were multiple phases including un-reacted oxide.

FUTURE WORK

Data on the conductivity and optical transparency of these Fe substituted mayenite should be collected. With these measurements some correlations could be made for a better understanding of the atomic/defect structure of the material and its effect on the electrical and optical properties. These measurements should be collected on thin film samples.

LIST OF REFERENCES

1. Mark Z. Jacobson. Review of Solutions to Global Warming, Air Pollution, and Energy Security. Energy Environ. Sci., 2009, doi:10.1039/b809990C.

2. Abdelilah Slaoui and Reuben T. Collins, Advanced Inorganic Materials for Photovoltaics'. MRS Bulletin • Vol. 2 • March 2007 • www.mrs.org/bulletin.

3. Bertoni, Mariana Ines, Cage structure materials for n-type transparent conducting oxides Ph.D., Northwestern University, 2007, 218 pages; AAT 3251914.

4. Elias Burstein. Anomalous optical absorption limit in insb. Phys. Rev., 93(3):632–633, 1954.

5. T. S. Moss. The interpretation of the properties of indium antimonide. Proceedings.

6. www.eng.tau.ac.il/Review of TCO Thin Films.

7. Z. Zhao, N. Vinson, T. Neumuller, J.E. McEntyre, F. Fortunato, A.T. Hunt, G. Ganguly. Transparent conducting ZnO: **Al** films via CCVD for amorphous silicon solar cells,. Conference Record 2002.

8. Yutaka Furubayashia, Taro Hitosugi, Yukio Yamamoto, Kazuhisa Inaba, Go Kinoda and Yasushi Hirose, Toshihiro Shimada and Tetsuya Hasegawa. A transparent metal: Nb-doped anatase TiO2. APPLIED PHYSICS LETTERS **86**, 252101 s2005d.

9. http:pubs.usgs.gov/ds/200s/140.

10. http://en.wikipedia.org/wiki/Mayenite.

11. M. Lacerda, J. T. S. Irvine, F. P. Glasser, and A. R. West. High oxide ion conductivity in Ca12Al14O33. Nature, 332(6164):525–526, 1988.

12. Satoru Matsuishi, et al. High-Density Electron Anions in a Nanoporous Single Crystal: [Ca24Al28O64]4+(4*e*-), Science **301**, 626 (2003); DOI: 10.1126/science.1083842.

13. Sushko, P. V., Shluger, A. L., Hayashi, K., Hirano, M. & Hosono, H. (2003). Phys. Rev. Lett. 91, 126401-1-4.

14. Medvedeva, J. E. & Freeman, A. J. (2004). Appl. Phys. Lett. 85, 955–957.

15. Li, Z., Yang, J., Hou, J. G. & Zhu, Q. (2004). Angew. Chem. 43, 6479–6482.

16. Hans Boysen,, Ines Kaiser-Bischoff, Martin Lerc., Anion Diffusion Processes in O- and N-Mayenite Investigated by Neutron Powder Diffraction, Diffusion Fundamentals **8** (2008) 2.1 – 2.8 © 2008, H. Boysen.

17. J. L. Dye, Inorg. Chem. **36**, 3817 (1997).

18. K. Hayashi, S. Matsuishi, T. Kamiya, M. Hirano, and H. Hosono. Light-induced conversion of an insulating refractory oxide into a persistent electronic conductor. Nature, 419(6906):462–465, 2002.

19. M. Miyakawa, K. Hayashi, M. Hirano, Y. Toda, T. Kamiya, and H. Hosono. Fabrication of highly conductive 12CaO · 7Al2O3 thin films encaging hydride ions by proton implantation. Advanced Materials, 15(13):1100, 2003.

20. Y. Toda, M. Miyakawa, K. Hayashi, T. Kamiya, M. Hirano, and H. Hosono. Thin film fabrication of nano-porous 12CaO·7Al2O3 crystal and its conversion into transparent conductive films by light illumination. Thin Solid Films, 445(2):309–312, 2003.

21. Mariana I. Bertoni, Thomas O. Mason, Julia E. Medvedeva, Arthur J. Freeman, Kenneth R. Poeppelmeier, Bernard Delley. Tunable conductivity and conduction mechanism in an ultraviolet light activated electronic conductor. J. Appl. Phys. 97, 103713 "2005.

22. Osborn E. F. and Muan A. $CaO\text{-}Al_2O_3\text{-}SiO_2$. In Phase Equilibrium Diagrams of Oxide Systems, volume 1, page 219. American Ceramic Society, 1960.

23. H. Boysen*a;* I. Kaiser-Bischoff, M. Lerch, S. Berendts, M. Hoelzel and A. Senyshyn. Disorder and Diffusion in Mayenite, Vol. 117 (2010) ACTA PHYSICA POLONICA A No. 1.

24. Gaki, R. Chrysafi, G. Kakali, Chemical synthesis of hydraulic calcium aluminate compounds using the Pechini technique', Journal of the European Ceramic Society 27 (2007) 1781–1784.

25. H. Boysen, Kaiser-Bischoff, M. Lerch, S. Berendts, Börger, D. M. Trots, M. Hoelzel, A. Senyshyn, Structures and properties of variously doped Mayenite investigated by neutron and synchrotron powder diffraction. Z. Kristallogr. Suppl. **30** (2009) 323-328 / **DOI** 10.1524/zksu.2009.0047.

26. R. R. Dayal and F. P. Glasser. Phase Relations in the System $CaO-Al_2O_3-Fe_2O_3$. Sci. Ceram. 1967.

27. Mohamed N. Rahaman. 'Ceramic Processing', CRC Press, 2007 Taylor anf Francis Group. ISBN 10:0-8493-7285-2.

28. Anthony K. Cheetham* and Caroline F. Mellot. In Situ Studies of the Sol-Gel Synthesis of Materials', Chem. Mater. **1997,** *9,* 2269-2279.

29. M Zahedi, A K Ray and D S Barratt. Preparation and crystallization of sol–gel C12A7 thin films, J. Phys. D: Appl. Phys. **41** (2008) 035404 (5pp).

30. B.H. Toby, "EXPGUI, a graphical user interface for GSAS", *J. Appl. Cryst.*, **34**, 210-213 (2001).

31. A.C. Larson and R.B. Von Dreele, "General Structure Analysis System (GSAS)", Los Alamos National Laboratory Report LAUR 86-748 (2000).

32. L. B. McCusker, R. B. Von Dreele, D. E. Cox, D. Louer and P. Scardi, "Rietveld refinement guidelines". J. Appl. Cryst., **32**, 36-50 (1999).

VITA

Sabina was born and grew up in Nigeria, she attended a special school of science (St. Cyprian's Special Science School Nsukka, Enugu State, Nigeria) during high school, and proceeded to get a bachelors degree in Metallurgical and Material Engineering at Enugu State University of Science and Technology Enugu, Nigeria, in December 2000.

After eight years of raising a family and working part time as a substitute teacher in the State of Connecticut, she went back to get a Masters degree in Materials Science and Engineering at the University of Tennessee Knoxville, Tennessee, in August 2010. Sabina is continuing at the University of Tennessee and the department of Materials Science and Engineering for a doctorate degree, hoping to graduate in August 2012.